A semi-classical Floquet-NEGF approach to model photon-assisted tunneling in quantum-well devices

Nathan De Sutter[1], Emile Vanderstraeten[1], Dries Vande Ginste[1]

[1]quest, IDLab, Dept. of Information Technology, Ghent University/imec, Belgium.

Corresponding author: Nathan.DeSutter@UGent.be;

Abstract

The non-equilibrium Green's function formalism is often employed to model photon-assisted tunneling processes in opto-electronic quantum well devices. For this purpose, self-consistent schemes based on a quantum electrodynamical description of light-matter interactions have been proposed before. However, these schemes are typically computationally very demanding. Therefore, in this work, a novel semi-classical method based on Floquet-Green theory is proposed, which strongly mitigates the computational costs. By comparison to results obtained with a traditional, purely quantum mechanical technique, the new approach is validated and shown to be faster and exhibits superior convergence properties. Finally, a two-band model for superlattice structures is constructed to further illustrate the advantages of the novel, advocated method.

Keywords: NEGF, Floquet-Green, Photon-assisted tunneling, Quantum well devices

1 Introduction

Multi-quantum well (MQW) devices have been the subject of extensive research since their inital proposition in 1970 by Esaki and Tsu [1]. Typically, these devices are layered structures that consist of an alternation of distinct semiconductors, as shown in Fig. 1. The multi-barrier potential energy profile U in the device gives rise to tunneling properties, leading to the manifestation of negative differential resistance. Initially, this prioritized their use as resonant tunneling diodes [2–4]. However, the past decades, the compact size and fast switching properties of quantum wells have also aroused interest in their opto-electronic features [5]. Several applications have been proposed, such as infrared photodetectors [6], waveguide modulators [7–9], light-emitting diodes [10–13], quantum cascade lasers [14–17] and solar cells [18, 19].

The development of these new MQW-based technologies requires specific modeling techniques that are able to simulate electron tunneling, which is a purely quantum mechanical phenomenon. Moreover, the often strong light-matter interactions in these novel devices demand to go beyond equilibrium assumptions. A method that meets both of these requirements is the non-equilibrium Green's function formalism (NEGF), which was pioneered in the 60s by Schwinger, Kadanoff-Baym and Keldysh [20–22]. This many-body physics based solution tool allows the calculation of device properties based on the Hamiltonian of the device and it has been applied broadly to the modeling of, e.g., atoms [23], nanojunctions [24, 25], transistors [26], quantum dots [27, 28] and carbon nanodevices [29–32].

Several NEGF-based models for opto-electronic MQW devices have been proposed

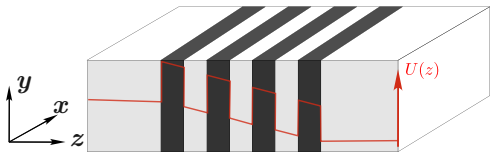

Fig. 1: Schematic representation of a multi-quantum well device. The red curve represents the potential energy profile in the structure.

before [33–36], which are based on a rigorous, second-quantized description of electron-photon interactions. Nevertheless, the computationally intensive nature of the resulting self-consistent schemes has limited their widespread application. In particular, the modeling of large intricate structures necessitates the introduction of significant approximations.

In this work, a novel semi-classical approach to include electron-photon interactions is proposed, based on Floquet-Green theory [37–42]. The self-energy convergence loop that is required in the fully quantum mechanical approaches is replaced by a basis expansion in Floquet harmonics [43] which strongly mitigates the computational load. Typically, Floquet-Green theory is used to study the AC response of systems connected to an external voltage source. Here, however, a novel NEGF method is employed as a new technique to study interactions between MQW devices and semi-classical light sources, which enables a direct comparison to models based on quantum electrodynamics. Moreover, the novel formalism allows for the efficient modeling of intricate two-band structures.

The paper is structured as follows. First, the choice of Hamiltonian for MQW devices is presented in Sec. 2. Thereafter, the previously established, fully quantum mechanical NEGF approach is briefly discussed in Sec. 3. Next, the new solution technique is detailed in Sec. 4. In Sec. 5, both methods are compared and benchmarked, followed by the application of the advocated method to the two-band modeling of superlattice structures.

2 Multi-quantum well device modeling

The following Hamiltonian $\hat{H}$ with minimal coupling is proposed as a starting point to model MQW structures subjected to an electromagnetic field:

$$\hat{H} = \hat{H}_0 + \hat{H}_{\text{int}}, \tag{1}$$

$$\hat{H}_0 \equiv \hat{\vec{p}} \cdot \left(\frac{1}{2m_e} \hat{\vec{p}} \right) + \hat{U}(z), \tag{2}$$

$$\hat{H}_{\text{int}} \equiv \frac{e}{m_e} \hat{\vec{p}} \cdot \hat{\vec{a}} + \frac{e^2}{2m_e} \hat{\vec{a}}^2. \tag{3}$$

Here, $\hat{\vec{p}} = -i\hbar\vec{\nabla}$ and $\hat{\vec{a}}$ represent the momentum operator and magnetic vector potential operator of the coupling electromagnetic field, whereas $\hat{U}(z)$ is the potential energy operator, consisting of the conduction band energy and the electrostatic potential energy. Furthermore, m_e represents the possibly z-dependent effective electron mass. Using transverse plane wave eigenstates, the three-dimensional non-interacting Hamiltonian $\hat{H}_0$ is reduced to one-dimensional contributions that are a function of the transverse wave vector $\mathbf{k}_\perp$ [44]. Since the methods described in this paper are independently applicable to these one-dimensional Hamiltonians, the final summation over $\mathbf{k}_\perp$-space that is required for the calculation of observables is not executed. Also, electron-phonon interactions are excluded, such that phonon-assisted energy relaxation [45] is not regarded. Issues with the resolution of bound states [46] are prevented by assuring sufficient coupling between the device and its contacts. Several basis representations in the longitudinal z-direction for the remaining $\hat{H}_0$ exist, depending on the amount of molecular information of the device that is to be included. First, an effective mass tight-binding model corresponding to the real-space basis $|z\rangle$ is obtained using a finite-difference approximation of the involved derivatives. This results in the following tridiagonal matrix representation (denoted in bold):

$$\mathbf{H}_0 = \begin{bmatrix} \ddots & & & \\ & \frac{2t}{m^*_{e,i-1}} + U_{i-1} & -\frac{t}{m_{e,i-1}} & 0 \\ & -\frac{t}{m_{e,i-1}} & \frac{2t}{m^*_{e,i}} + U_i & -\frac{t}{m_{e,i}} \\ & 0 & -\frac{t}{m_{e,i}} & \frac{2t}{m^*_{e,i+1}} + U_{i+1} \\ & & & \ddots \end{bmatrix}, \tag{4}$$

where $m_{e,i}$ and U_i represent the discretized electron's effective mass and potential energy at

$z = i\Delta z$, respectively. Furthermore, $m^*_{e,i} = 2\frac{m_{e,i}m_{e,i-1}}{m_{e,i}+m_{e,i-1}}$ is the harmonic mean of the effective mass and $t \equiv \frac{\hbar^2}{2\Delta z^2}$.

Alternatively, and as was used in this work, semi-empirical planar orbital basis sets that depict the molecular nature of the involved semiconductors can be employed to obtain a *multi-band* representation of the device [47]. To this end, the slab-like geometry of the quantum-well device is divided into layers containing several atoms. The coupling of the atoms' orbitals then gives rise to the band-structure of the semiconductor. By only taking into account interactions between neighboring layers, the following tridiagonal block-matrix structure is obtained [33]:

$$\mathbf{H}_0 = \begin{bmatrix} \ddots & & & \\ & \mathbf{E}_{i-1} & \mathbf{V}^{ac}_{i-1} & 0 \\ & \mathbf{V}^{ca}_{i-1} & \mathbf{E}_i & \mathbf{V}^{ac}_i \\ & 0 & \mathbf{V}^{ca}_i & \mathbf{E}_{i+1} \\ & & & \ddots \end{bmatrix}. \tag{5}$$

Here, $\mathbf{E}_i$ corresponds to the on-site energy matrix at layer i, whereas $\mathbf{V}^{ac}_i = (\mathbf{V}^{ca}_i)^\dagger$ is the anion-cation coupling matrix at layer i. If a two-band model is constructed, all block-matrix elements $\mathbf{E}_i$, $\mathbf{V}^{\mathrm{ca}}_i$ have dimensions 2×2. Thus, a similar tridiagonal structure as the previous representation (4) is observed, albeit with an extension of the basis.

3 Non-equilibrium Green's function formalism

The basic quantity in the NEGF formalism is the single-particle Green's function $g(1, 1')$, which can be interpreted as a response function that carries information on the propagation of a particle from space-time coordinate $1' = (\mathbf{r}'_1, t'_1)$ to $1 = (\mathbf{r}_1, t_1)$. In practice, $g(1, 1')$ is fully determined by introducing four different real-time Green's functions, namely the retarded/advanced Green's functions $g^{R/A}(1, 1')$ and the lesser/greater Green's functions $g^{\lessgtr}(1, 1')$. Knowledge of these quantities allows the calculation of interesting one-body observables, such as the particle density and current. In this section, the basic equations that govern the NEGF formalism, as well as the fully quantum mechanical solution scheme reported in [33, 34] are briefly outlined.

3.1 Equations of motion

The real-time Green's functions $g^{R/A}$ and $g^{\lessgtr}$ are generally calculated from the time-dependent Kadanoff-Baym equations [20]:

$$\left(i\hbar\frac{\partial}{\partial t_1} - \hat{H}_0\right) g^{R/A}(1, 1') = \delta(1, 1') + \int \mathrm{d}2\ \Sigma^{R/A}(1, 2) g^{R/A}(2, 1'), \tag{6}$$

$$g^{\lessgtr}(1, 1') = \int \mathrm{d}2 \int \mathrm{d}3\ g^R(1, 2)\Sigma^{\lessgtr}(2, 3)g^A(3, 1'). \tag{7}$$

Since only *steady-state* properties are of interest in this section, all involved Green's functions only depend on time differences $\tau = t_1 - t'_1$. As a result, the Fourier transform can be introduced:

$$g^{R/A,\lessgtr}(\tau) = \frac{1}{2\pi\hbar}\int \mathrm{d}E\ e^{-iE\tau/\hbar} G^{R/A,\lessgtr}(E). \tag{8}$$

Note that time-dependent functions are denoted by small letters, whereas energy-dependent functions are denoted by capital letters. By applying the Fourier transform (8) to the Kadanoff-Baym equations (6)-(7), the following equations of motion are obtained upon projecting on a real-space basis [36]:

$$\mathbf{G}^{R/A} = \mathbf{G}^{R/A}_0 + \mathbf{G}^{R/A}_0 \mathbf{\Sigma}^{R/A} \mathbf{G}^{R/A}, \tag{9}$$

$$\mathbf{G}^{\lessgtr} = \mathbf{G}^R \mathbf{\Sigma}^{\lessgtr} \mathbf{G}^A. \tag{10}$$

These are named Dyson's equation and Keldysh' equation respectively. The self-energies $\mathbf{\Sigma}^{R/A;\lessgtr}$ determine the types and order of interactions that are included in the model. The difficulty in calculating the Green's functions thus lies in obtaining an adequate approximation for these self-energies. In this work, the focus is on electron-photon interactions, denoted as $\mathbf{\Sigma}_{\mathrm{ep}}$ and derived from the interaction Hamiltonian $\hat{H}_{\mathrm{int}}$ of the system, and on boundary contributions owing to the coupling of the device to contacts α, denoted as $\mathbf{\Sigma}_\alpha$, such

that:

$$\mathbf{\Sigma}^{R/A;\lessgtr}(E) = \sum_{\alpha} \mathbf{\Sigma}_{\alpha}^{R/A;\lessgtr}(E) + \mathbf{\Sigma}_{\mathrm{ep}}^{R/A;\lessgtr}(E). \quad (11)$$

If all interactions are neglected, the device is described by the *non-interacting Green's functions* $\mathbf{G}_0^{R/A}$:

$$\left[E\mathbf{I} \pm i\eta - \mathbf{H}_0\right] \mathbf{G}_0^{R/A}(E) = \mathbf{I}. \quad (12)$$

Finally, for systems where time-reversal holds, the retarded and advanced Green's functions are linked through:

$$\mathbf{G}^{R}(E) = \left[\mathbf{G}^{A}(E)\right]^{\dagger}. \quad (13)$$

3.2 Self-energies

Expressions for the electron-photon self-energies are typically derived from quantum electrodynamics (QED). By assuming a weak electric field, only the first-order term in the vector operator $\hat{\vec{a}}$ is included in $\hat{H}_{\mathrm{int}}$:

$$\hat{H}_{\mathrm{int}} \approx \frac{e}{m_e} \hat{\vec{p}} \cdot \hat{\vec{a}}. \quad (14)$$

The following electron-photon self-energy matrix elements $\mathbf{\Sigma}_{ep;lm} \equiv \langle l| \Sigma_{ep} |m\rangle$ are then obtained according to [34]:

$$\begin{aligned}\mathbf{\Sigma}_{ep;lm}^{\lessgtr}(E) = \sum_{pq} M_{lp} M_{qm} [N_{\mathrm{ph}} \mathbf{G}_{pq}^{\lessgtr}(E \mp \hbar\omega) \\ + (N_{\mathrm{ph}} + 1) \mathbf{G}_{pq}^{\lessgtr}(E \pm \hbar\omega)],\end{aligned} \quad (15)$$

$$M_{lp} \equiv \begin{cases} \frac{e\hbar}{2im_e(z_p - z_l)} \sqrt{\frac{\hbar\sqrt{\mu_r\epsilon_r}}{2N_{\mathrm{ph}}\omega\epsilon c} I_{\omega}} & |p-l| = 1 \\ 0 & \text{else} \end{cases}. \quad (16)$$

Where $\mathbf{G}_{pq}^{\lessgtr} \equiv \langle p| G^{\lessgtr} |q\rangle$, with $|p\rangle$ corresponding to real-space site $p\Delta z$ and where N_{ph} represents the photon number, $\hbar\omega$ the photon energy, ϵ and μ the dielectric permittivity and magnetic permeability, respectively and I_{ω} the photon flux. The N_{ph}-term in (15) encompasses absorption, whereas the $(N_{\mathrm{ph}} + 1)$-term describes spontaneous and stimulated emission. Moreover, in steady-state, the electron-photon self-energies are calculated by means of a Hilbert transformation:

$$\mathbf{\Sigma}_{\mathrm{ep}}^{R/A}(E) = i \lim_{\eta \to 0^+} \int \frac{\mathrm{d}E'}{2\pi} \frac{\mathbf{\Sigma}_{\mathrm{ep}}^{>}(E') - \mathbf{\Sigma}_{\mathrm{ep}}^{<}(E')}{E - E' \pm i\eta}. \quad (17)$$

Within the *self-consistent Born approximation* (SCBA), the self-energies in (15) are dependent on the *fully* interacting Green's functions $\mathbf{G}^{R/A,\lessgtr}$, which in their turn are calculated from the self-energies. This results in a self-consistent solution method.
Finally, the boundary self-energies $\mathbf{\Sigma}_{\alpha}$ are calculated from surface Green's functions, which are obtained through the Sancho-Rubio scheme [48]. Alternative approaches leverage the established transfer-matrix method [49] or complex absorbing potentials [50].

3.3 Derivative quantities

Determining the self-energies and the fully interacting Green's functions $\mathbf{G}^{R/A,\lessgtr}$ yields the electron density in the device, n, and steady-state current through contact α, I_{α} [51, 52]:

$$n(k\Delta z) = -2i \int \frac{\mathrm{d}E}{2\pi} \mathbf{G}_{kk}^{<}(E), \quad (18)$$

$$\begin{aligned} I_{\alpha} = \frac{2e}{\hbar} \int \frac{\mathrm{d}E}{2\pi} [\mathbf{\Sigma}^{R}\mathbf{G}^{<} - \mathbf{G}^{R}\mathbf{\Sigma}^{<} \\ + \mathbf{\Sigma}^{<}\mathbf{G}^{A} - \mathbf{G}^{<}\mathbf{\Sigma}^{A}]_{\alpha,\alpha;E}. \end{aligned} \quad (19)$$

Moreover, the local density-of-states (LDOS) D of electrons in the device is defined as:

$$D(E, k\Delta z) \equiv \frac{i}{2\pi} \left[\mathbf{G}^{R}(E) - \mathbf{G}^{A}(E)\right]_{kk}. \quad (20)$$

3.4 Solution scheme

The self-consistent method [33] is schematically represented in Fig. 2 and this reference method is from now on referred to as *QED-NEGF*. It consists of an iterative self-energy convergence loop, as well as a self-consistent Poisson-Schrödinger solver [44]. The latter involves updating the potential energy profile $U(z)$ via the calculated electron density. This is not of importance for the purposes of this paper, and will not be executed. The iteration scheme for the self-energies goes as follows:

1. Calculate $\mathbf{G}_0^{R/A}$ from (12), using the initialized potential energy profile $U(z)$ and boundary self-energies $\boldsymbol{\Sigma}_{\boldsymbol{\alpha}}^{\boldsymbol{R/A},\lessgtr}$.
2. Calculate $\mathbf{G}^{\lessgtr}$ using $\mathbf{G}^{R/A}$ and $\boldsymbol{\Sigma}^{\lessgtr}$ in (10).
3. Update $\boldsymbol{\Sigma}_{\mathrm{ep}}^{\lessgtr}$ using (15).
4. By invoking (17), calculate $\boldsymbol{\Sigma}_{\mathrm{ep}}^{R/A}$, in order to update $\mathbf{G}^{R/A}$ using (9). This closes the iteration loop.

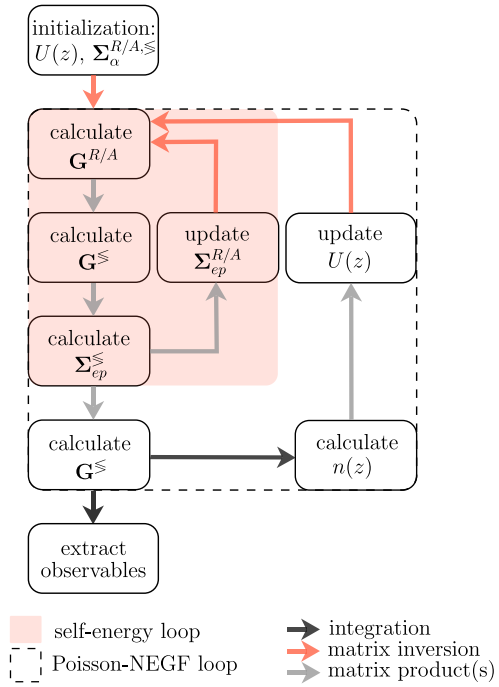

Fig. 2: Flowchart of the QED-NEGF reference solution method.

Several cumbersome calculations are required in this scheme. First, all Green's functions matrix elements are needed to update the electron-photon self-energies. Therefore, recursive methods [53] — often applied to mitigate the computational demands of NEGF approaches — which only require a limited amount of matrix elements, are not feasable. Furthermore, the determination of self-energies corresponding to energy E, is based on Green's functions evaluated at shifted energies $E \pm \hbar\omega$. Performing iteration loops therefore requires knowledge of Green's functions in different, shifted energy intervals, which complicates energy discretization. Finally, electron-photon self-energies obtained using (15) are not sparse, such that the tridiagonal nature of the initial non-interacting Green's function is lost by including $\boldsymbol{\Sigma}_{\mathrm{ep}}^{R/A}$. This also complicates the matrix products in Keldysh' equation.

4 Semi-classical Floquet-Green approach

Photon-assisted tunneling in MQW devices is based on absorption and stimulated emission processes, the modeling of which does not necessarily require a rigorous quantum mechanical treatment of the coupled light. Especially in the case of weak electromagnetic fields, the dominating tunneling mechanisms do not include intricate electron-photon interactions. Therefore the new semi-classical approach that is presented in this section suffices and will be demonstrated to outperform more traditional methods. The novel solution scheme is based on Floquet-Green theory, and allows to mitigate most of the numerical difficulties of the QED-NEGF method that were discussed above. The advocated scheme will be referred to as *Floquet-NEGF*.

The semi-classical treatment is constructed within the *long-wavelength approximation* and by choosing the *velocity gauge*, which is explained in Appendix A. As such, the following interaction Hamiltonian is obtained:

$$\hat{h}_{\mathrm{int}}(t) = \frac{e}{m_e}\hat{\vec{p}}\cdot\vec{a}(t), \tag{21}$$

where the magnetic vector potential reduces to an explicitly time-dependent vector $\vec{a}(t)$ and its quadratic term is eliminated by the choice of gauge. Assuming an electric field with angular frequency ω that is linearly polarized along the z-axis leads to the following full Hamiltonian $\hat{h}(t)$:

$$\hat{h}(t) = \hat{H}_0 + A_0\cos(\omega t)\hat{p}_z. \tag{22}$$

From classical considerations, included in Appendix A, an expression for A_0 as a function of the photon flux I_ω is retrieved:

$$A_0 = \frac{2e}{m_e}\sqrt{\frac{\hbar I_\omega}{\epsilon c\omega}}. \tag{23}$$

In Sec. 3, the interaction Hamiltonian was split from the non-interacting one and gave rise to the

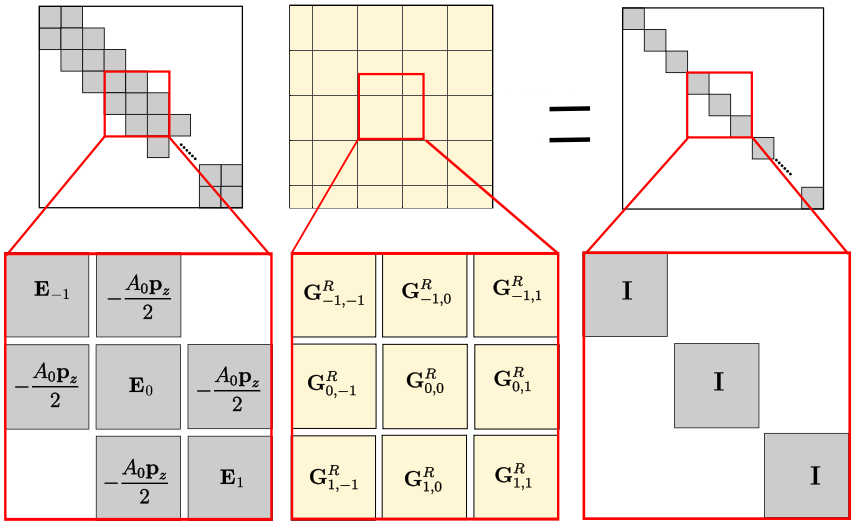

Fig. 3: Schematic of the Floquet-NEGF matrix equation (25).

electron-photon self-energy expressions. Here on the other hand, the *full* Hamiltonian $\hat{h}(t)$ (22) is employed in the time-dependent Kadanoff-Baym equations (6)-(7). The remaining self-energies in these expressions now only stem from device-lead coupling. Since (8) can no longer be applied, the difficulty is thus shifted to treating the explicit time-dependence of $\hat{h}(t)$. To this end, the two-time Fourier transform is introduced:

$$\mathbf{g}^{R/A,\lessgtr}(t_1,t_1') = \int \frac{\mathrm{d}E_1}{2\pi\hbar}\int \frac{\mathrm{d}E_1'}{2\pi\hbar}\boldsymbol{\mathcal{G}}^{R/A,\lessgtr}(E_1,E_1') e^{-\frac{i}{\hbar}(E_1t_1-E_1't_1')}, \tag{24}$$

as well as an expansion in Floquet harmonics, based on the periodicity of the Hamiltonian. After some tedious calculations, which are detailed in Appendix *B*, alternative expressions for Dyson's and Keldysh' equations emerge:

$$[E\mathbf{I}-\mathbf{H}_0-\sum_\alpha \mathbf{\Sigma}^R_\alpha(E)]\mathbf{G}^R_{0,n}(E) - \frac{A_0\mathbf{p}_z}{2}\left[\mathbf{G}^R_{-1,n}(E)+\mathbf{G}^R_{1,n}(E)\right] = \delta_{n,0}\mathbf{I}, \tag{25}$$

$$\mathbf{G}^<_{0,n}(E) = \sum_\alpha\sum_m \mathbf{G}^R_{0,m}(E)\mathbf{\Sigma}^<_\alpha(E+m\hbar\omega)\mathbf{G}^A_{m,n}(E). \tag{26}$$

Here, the matrix elements $\mathbf{p}_{z,lm} = \langle l|\,\hat{p}\,|m\rangle$ in the real-space basis take the following form through invoking Heisenberg's equation [33, 54]:

$$\mathbf{p}_{z,lm} = \frac{im_e(z_m-z_l)}{\hbar}\mathbf{H}_{0,lm}, \tag{27}$$

where $z_m - z_l$ represents the distance between two real-space nodes or layers. Also, the following notation for the involved Floquet harmonics was introduced:

$$\mathbf{G}^{R,<}_{m,n}(E) \equiv \mathbf{G}^{R,<}(E+m\hbar\omega, E+n\hbar\omega). \tag{28}$$

It should be noted that advanced harmonics $\mathbf{G}^A_{m,n}$ are readily obtained from retarded harmonics $\mathbf{G}^R_{m,n}$ by invoking (13).
Similar considerations lead to the following equations for the current through lead α:

$$I_\alpha = I_\alpha^{\mathrm{cond}} + I_\alpha^{\mathrm{pump}}, \tag{29}$$

$$I_\alpha^{\mathrm{cond}} \equiv \frac{2e}{\hbar}\int\frac{\mathrm{d}E}{2\pi}T_{\alpha\beta}(E)(f_\alpha(E)-f_\beta(E)), \tag{30}$$

$$I_\alpha^{\mathrm{pump}} \equiv \frac{2e}{\hbar}\int\frac{\mathrm{d}E}{2\pi}(T_{\beta\alpha}(E)-T_{\alpha\beta}(E))f_\alpha(E), \tag{31}$$

$$T_{\alpha\beta}(E) \equiv \sum_n \mathrm{Tr}[\mathbf{G}^A_{0,n}(E)\mathbf{\Gamma}_\alpha(E+n\hbar\omega)\mathbf{G}^R_{n,0}(E)\mathbf{\Gamma}_\beta(E)], \tag{32}$$

where the broadening function $\mathbf{\Gamma}_\alpha \equiv i(\mathbf{\Sigma}_\alpha^R - \mathbf{\Sigma}_\alpha^A)$ was introduced. The two contributions I_α^{cond} and I_α^{pump} correspond to a conduction current similar to the Landauer-Büttiker formula and a pumped current owing to electron-photon interactions, respectively [41, 55]. Both are dependent on the transmission function $T_{\alpha\beta}(E)$ for quantum transport between leads α and β. For symmetric structures, where $T_{\beta\alpha}(E) = T_{\alpha\beta}(E)$, it is clear that the pumped current disappears. This enforces the necessity of symmetry breaking in photodetectors by, e.g., applying a bias voltage or embedding a terminating barrier.

The solution scheme now becomes apparent by noting that $\mathbf{G}_{m,n}^{R/A,\lessgtr}(E + k\hbar\omega) = \mathbf{G}_{m+k,n+k}^{R/A,\lessgtr}(E)$. Evaluating (25) at $E \to E + n\hbar\omega$ ($n \in \mathbb{Z}$) leads to an infinite set of implicit matrix equations. Schematically, this set of equations is illustrated by Fig. 3. The left matrix represents a tridiagonal block-matrix, with diagonal blocks of size $N \times N$:

$$\mathbf{E}_n \equiv (E + n\hbar\omega)\mathbf{I} - \mathbf{H}_0 - \sum_\alpha \mathbf{\Sigma}_\alpha^R(E + n\hbar\omega), \quad (33)$$

and off-diagonal blocks $-\frac{A_0\mathbf{p}_z}{2}$. The inversion of the left block-matrix results in the middle block-matrix with Floquet harmonics $\mathbf{G}_{i,j}^R(E)$, which are required in (32). In practice, the matrix equation (25) needs to have finite dimensions. Therefore, the number of Floquet modes is truncated to M, an odd number, leading to $M \times M$ blocks in (25). This implies that a real-space basis set of size N results in an overall matrix dimensionality of $(MN) \times (MN)$.

The Floquet-NEGF method is schematically drawn in Fig. 4, and consists of the following steps:

1. Initialize the block-matrix dimension M, the potential energy profile $U(z)$ and the boundary self-energies $\mathbf{\Sigma}_{\boldsymbol{\alpha}}^{\boldsymbol{R/A,\lessgtr}}$.
2. Calculate $\mathbf{G}^R$ from (25), and thus from the solution scheme shown in Fig. 3.
3. Calculate the current I_α from (29), using the required device-lead coupling self-energies.
4. If desired, e.g., to self-consistently solve Poisson's equation, calculate the electron density n with the $\mathbf{G}_{0,0}^<$-matrix obtained from (26), analogously to (18).
5. Check convergence by increasing M at least once.

The advantage over the QED-NEGF of Sec. 3 approach is immediately visible, since the self-energy loop, which requires cumbersome matrix products, is eliminated. Instead, M should be chosen large enough, to ensure convergence. The sparsity of the involved matrices is kept, and shifting of energy intervals no longer complicates the scheme as was the case for the traditional method. Furthermore, since only $\mathbf{G}_{n,0}^R(E)$-matrices are required in (32), it is not necessary to invert the full block-matrix. Instead, the system of equations can be partially solved.

5 Results and discussion

5.1 Resonant tunneling diode

5.1.1 Validation

Both approaches are now compared through the modeling of the resonant tunneling diode (RTD) that was discussed in [34]. To construct an effective mass model, the material parameters shown in Table 1 are employed. Here, U_{barrier} refers to the applied terminating barrier, which is visible in the LDOS of the structure, shown in Fig. 5*a*. Although electron-phonon interactions were neglected, it is clear that the sufficient resolution of the confined energy levels is assured because of broadening induced by the contacts. Based on this figure, it

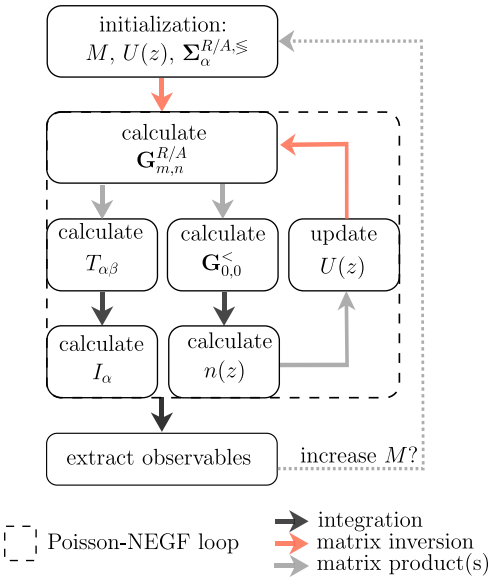

Fig. 4: Flowchart of the Floquet-NEGF solution method.

Table 1: Parameters used for the RTD simulation, as reported in [34]

Material parameter	
Δz	1 Å
μ	0.17 eV
ϵ	12.9 ϵ_0
m_e	0.067 m_0
I_ω	1000 W/m^2
U_{barrier}	0.2 eV

is also clear that the Fermi level was chosen such that only the ground-state energy level is occupied. The photocurrent response function R of this device, defined as

$$R = \frac{I_\alpha^{\text{pump}}}{qI_\omega}, \tag{34}$$

is presented in Fig. 5*b* for both methods. For the QED-NEGF simulation, only absorption contributions to $\mathbf{\Sigma}_{\text{ep}}^{\lessgtr}$ were included in (15) owing to the choice of Fermi level, and the method converged after one iteration. Floquet-NEGF clearly reproduces the same result and converges already for block-matrix dimension $M = 3$. The photocurrent equals zero for $M = 1$, such that this result was not included in the figure. Moreover, both methods match the results that were presented in [34], which serves as an extra validation. The three peaks that are visible in the photocurrent response function of the device correspond to transitions originating from the ground-state energy level $E_0 \approx 0.15$ eV, given its occupation. The second peak, which stems from the $E_0 \to E_2$ transition, is suppressed with respect to the other ones due to selection rules. This example will now be employed to further compare both methods.

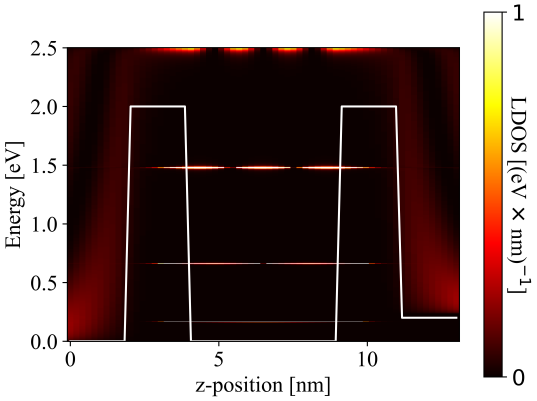

(a) Local density-of-states. The white contour corresponds to the conduction band profile.

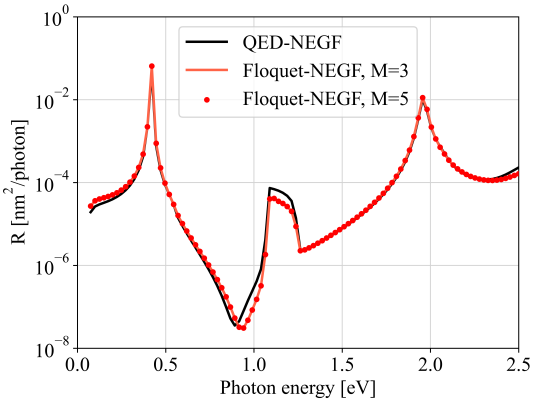

(b) Photocurrent response function simulations performed by the QED-NEGF and Floquet-NEGF approach.

Fig. 5: Simulations performed for the RTD structure presented in [34].

5.1.2 Inclusion of more-photon processes

The fundamentally different inclusion of electron-photon processes calls for a careful comparison. The QED-NEGF approach treats the interaction Hamiltonian by means of electron-photon self-energies. However, the traditional QED-NEGF expressions only encompass the Fock term, corresponding to one-photon processes [56]. If the self-energy iteration loop is not performed, the method is limited to modeling one-photon absorption and emission. Iterations sequentially include more-photon processes, according to the SCBA. Nevertheless, this renders the method computationally intractable, as explained before.
Floquet-NEGF, on the other hand, requires solving an infinite implicit set of equations. A truncation to $M \times M$ blocks in the matrix system, is performed, such that only $\mathbf{G}_{k,0}^R$-terms, where $k \in (-k_{\max}, \ldots, k_{\max})$ with $k_{\max} = \frac{M-1}{2}$, are included in the pumped current (31). Since these terms correspond to electrons undergoing $E + k\hbar\omega \to E$ transitions, k-photon processes are taken into account. As a result, more-photon processes can

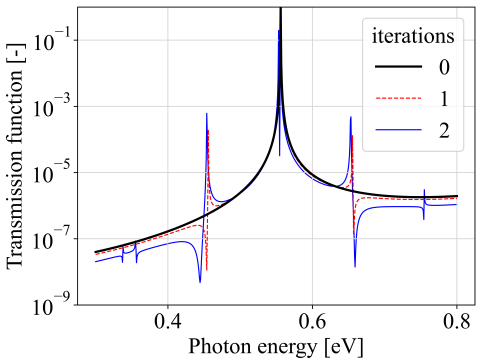

(a) QED-NEGF method.

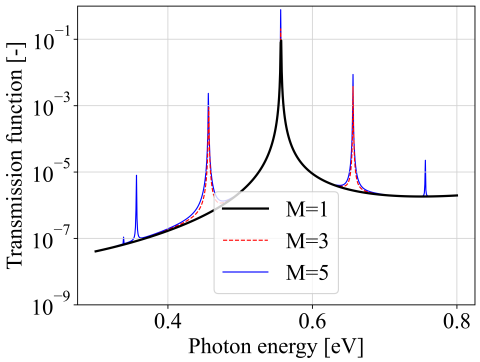

(b) Floquet-NEGF method.

Fig. 6: Transmission functions obtained through both methods for different degrees in inclusion of electron-photon interactions. The photon energy equals 0.1 eV and $I_\omega = 10^{11}\ W/m^2$.

be systematically incorporated by increasing the dimensions of the block-matrix system.

These claims are now corroborated by studying the transmission function of the RTD for a high photon flux $I_\omega = 10^{11}\ W/m^2$ and photon energy $\hbar\omega$=0.1 eV, as shown in Fig. 6. Including first-order electron-photon interactions, corresponding to either performing a single iteration loop in QED-NEGF or solving a (3×3)-block matrix system in Floquet-NEGF, results in additional peaks near the first excited energy state $E_1 \approx 0.56$ eV. These peaks are situated at $E_1 \pm \hbar\omega$, as expected. Similarly, second-order interactions give rise to peaks at $E_1 \pm 2\hbar\omega$, confirming the inclusion of two-photon processes for both methods. However, it is clear that the shape and intensity of the additional peaks obtained with QED-NEGF differ from the Floquet-NEGF result. This is readily explained as follows. The high photon flux is necessary to observe the second-order peaks, which correspond to two-photon processes with low-probability. These high intensity simulations, however, violate both the perturbative nature of the SCBA [57] and the first order approximation (14) in the interaction Hamiltonian. On the other hand, the Floquet-NEGF method does not include a low-intensity approximation. The interaction Hamiltonian is similar to (14), but merely because of the employed velocity gauge. The comparison here is thus necessarily somewhat limited, still pointing out that the additional peaks are observed at the correct locations for both methods and that the Floquet-NEGF technique converges excellently.

5.1.3 Computational demands

The calculation of the photocurrent response function R is now used to benchmark the computation times of both methods. All simulations are performed on a CPU laptop with 16 GB of RAM memory. The total computation time, t_{tot}, is composed of the time required to perform all matrix inversions, t_{inv}, and all matrix products, t_{prod}. The results are presented in Fig. 7. On the one hand, N corresponds to the number of real-space grid steps, which characterizes the basis size. On the other hand, the number of energy steps N_E determines the coarseness of the energy discretization. Figures 7*a* and 7*c* display computation times for both methods, including first-order electron-photon interactions. It is clear that t_{prod} fully determines the total required computation time t_{tot} for the QED-NEGF method, since both the full black line and the dashed black line coincide. This is understood from Fig. 2, where Keldysh' equation is employed to update $G^<$. The long computation times are caused by the dense self-energy matrices that are involved in these matrix products. In contrast, the equivalent Dyson's and Keldysh' equations for the Floquet-NEGF method, (25) and (26) respectively, are entirely determined by the Floquet harmonics $G^R_{m,n}$, requiring block matrix inversions. Consequently, t_{prod} remains low for this method and the matrix inversion time is expected to be the decisive factor. However, because of the sparsity of

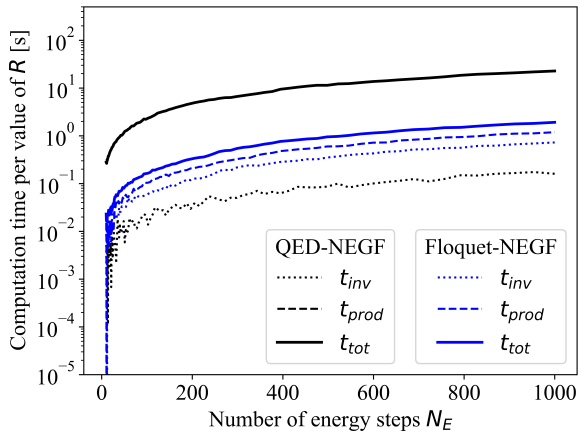

(a) Computation times as a function of N_E, including first-order electron-photon interactions. The number of sites is fixed at $N = 50$.

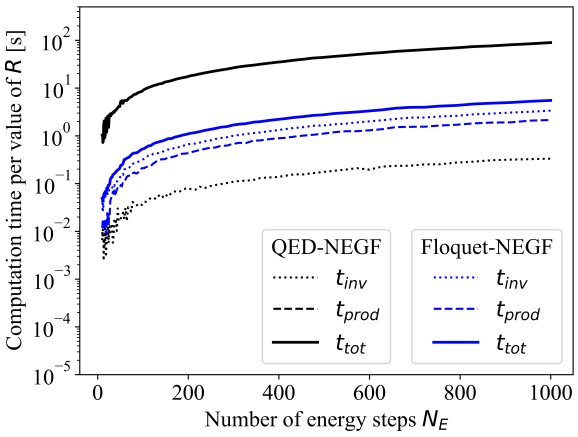

(b) Computation times as a function of N_E, including second-order electron-photon interactions. The number of grid steps is fixed at $N = 50$.

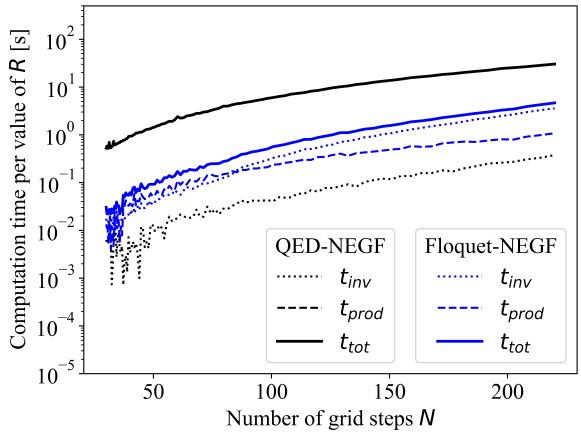

(c) Computation times as a function of N, including first-order electron-photon interactions. The number of energy steps is fixed at $N_E = 50$.

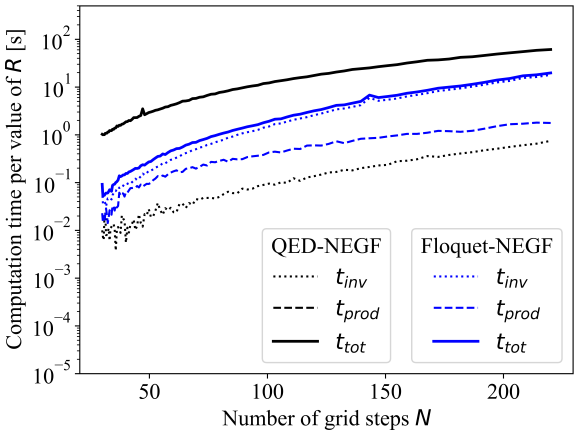

(d) Computation times as a function of N, including second-order electron-photon interactions. The number of energy steps is fixed at $N_E = 50$.

Fig. 7: Computation times per data point of the photocurrent response function. The total time t_{tot} consists of the matrix inversion time t_{inv} and the matrix product time t_{prod}. Note that t_{tot} (full black line) and t_{prod} (dashed black line) overlap for the QED-NEGF case.

the matrices involved and since not all matrix elements need to be determined, as mentioned before, t_{inv} remains low.

Identical trends are visible in Figs. 7*b* and 7*d*, where second-order interactions are included. The computation times for Floquet-NEGF are obviously somewhat higher due to the increase in t_{inv}, but still remain significantly lower than QED-NEGF. This could perhaps even be further improved upon by implementing recursive methods. Finally, it should be noted that the total computation time, t_{tot}, of both methods is more sensitive to the size of the basis than to the number of energy discretisation steps.

Since Floquet-NEGF proves to be considerably faster, it is therefore better suited to model intricate devices. This is the subject of the following section.

5.2 Expansion to two-band modeling of multi-quantum well structures

The effective mass model that was applied in all previous simulations is quite simplistic. In order to model interband transitions, expanding the theory to two-band descriptions should be considered. This increases the computational load, since the basis size is doubled according to (5). Moreover, an expansion to MQW models is required to describe superlattice structures [58, 59]. The advocated Floquet-NEGF method is capable of simulating such devices and will therefore be employed in what follows.

Table 2: Parameters used for the two-band simulations of MQW devices provided by [33].

Material parameter	Well	Barrier
ϵ	12.9 ϵ_0	13.1 ϵ_0
m_e	0.067 m_0	0.1087 m_0
E_{con}	0.5 eV	0.75 eV
E_{val}	0 eV	-0.15 eV
V_{ac}	2.5 eV	2 eV
ΔE	0.001 eV	
Δz	2 Å	
μ	0.6 eV	

A two-band model is obtained by making use of the material parameters provided in [33]. These are listed in Table 2, as well as the simulation parameters. Here, E_{con} and E_{val} represent conduction band and valence band energies, respectively. Furthermore, the extension to MQW devices is made. The resulting LDOS for single, three- and six-well structures are shown in Fig. 8. The periodic superlattice structure causes the formation of *minibands*. Because transitions between these minibands are now possible, additional peaks appear in the photocurrent response function, which is shown in Fig. 9*a*. Since the Fermi level was chosen to be $\mu = 0.6$ eV, these peaks correspond to $E_0 \to E_1$-transitions in the conduction band.

If now the Fermi level is chosen to be 0.2 eV, interband transitions take place. This is shown in Fig. 9*b* for the same MQW devices, where the peak for the single-well device occurs at photon energy $\hbar\omega \approx 0.61$ eV, as expected based on the

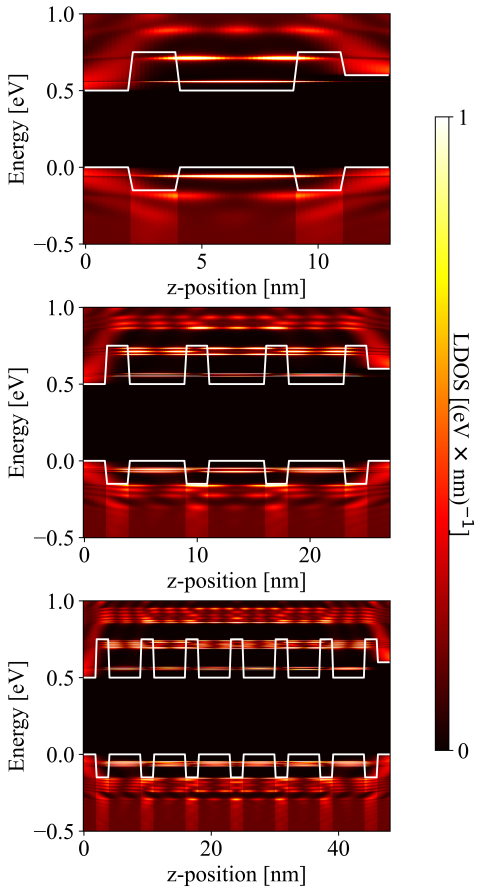

Fig. 8: LDOS of the two band models for the single-well device (top), the three-well device (middle) and the six-well device (bottom).

LDOS. Once again, minibands give rise to additional peaks. These results further illustrate the appositeness of the novel Floquet-NEGF method to model quantum-well devices.

6 Conclusion

In this paper, a novel approach based on Floquet-Green theory was proposed for the simulation of electron-photon interactions in multi-quantum well devices. To this end, a semi-classical model was constructed, allowing a linearly polarized electromagnetic field to interact with the structure. Choosing the velocity gauge in the long-wavelength approximation results in an explicitly time-dependent interaction Hamiltonian, similar

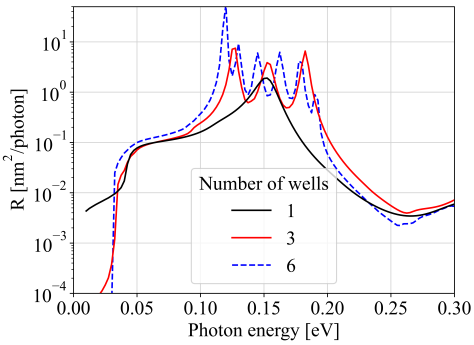

(a) Fermi level $\mu = 0.6$ eV.

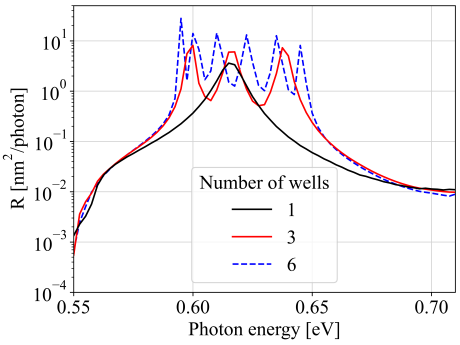

(b) Fermi level $\mu = 0.2$ eV.

Fig. 9: Photocurrent response functions R acquired from a two-band model for several superlattice structures and different Fermi levels.

to the established second-quantized NEGF methods, but without having to assume low field intensities. By introducing Floquet modes, a novel system of equations was obtained, which eliminates the need for a self-energy iteration loop that typically complicates other NEGF approaches. This novel method was then validated by reproducing the result from [34], which enabled a fair comparison between the QED-NEGF and Floquet-NEGF methods. Both were deemed capable of including higher-order electron-photon interactions, but Floquet-NEGF proved to be at least ten times faster. This allowed to simulate more elaborate two-band models of superlattice devices, which exhibit minibands owing to their periodicity, demonstrating the broad applicability of the advocated method. The results from this paper depict coherent transport, for which a Floquet scattering matrix approach [60] is a viable alternative. Nonetheless, for realistic devices, the full strength of NEGF methods, such as the one presented here, should to be exploited. Therefore, incoherent and phase-breaking interactions need to be included in the method. These additions, as well as a further study of the validity of conservation laws in our Floquet-NEGF approach pose interesting topics for future research.

Appendix A Velocity gauge

To embed electromagnetic fields in the quantum mechanical description of our systems, it suffices to introduce the following minimal coupling Hamiltonian:

$$\hat{h}(t) = \frac{(\hat{\vec{p}} + e\vec{a}(\vec{r},t))^2}{2m_e} - e\phi(\vec{r},t). \tag{A1}$$

The electromagnetic vector potential $\vec{a}(\vec{r},t)$ and scalar potential $\phi(\vec{r},t)$ are defined, using the electric field $\vec{e}(\vec{r},t)$ and magnetic field $\vec{b}(\vec{r},t)$ by the equations:

$$\vec{e}(\vec{r},t) = -\frac{\partial \vec{a}(\vec{r},t)}{\partial t} - \vec{\nabla}\phi(\vec{r},t), \tag{A2}$$

$$\vec{b}(\vec{r},t) = \vec{\nabla} \times \vec{a}(\vec{r},t). \tag{A3}$$

However, these potentials $\vec{a}$ and ϕ are not unique, thus switching to a different gauge with potentials $\vec{a}'$ and ϕ' is allowed under the following conditions:

$$\vec{a}' = \vec{a} - \vec{\nabla}\chi, \tag{A4}$$

$$\phi' = \phi + \frac{\partial \chi}{\partial t}, \tag{A5}$$

with *gauge transformation function* $\chi(\vec{r},t)$. Since, in this work, the impinging electromagnetic field is a monochromatic plane wave, linearly polarized along the z-direction, the electric field $\vec{e}$ is readily obtained:

$$\vec{e}(\vec{r},t) = e_0 \sin\big(\omega t - k_0\, \vec{r}\cdot\vec{u}_\parallel\big)\vec{u}_z. \tag{A6}$$

Now assume that the fields are initially described in the Lorenz gauge, denoted by the (L) superscript:

$$\vec{\nabla}\cdot\vec{a}^{(\mathrm{L})} + \frac{1}{c^2}\frac{\partial \phi^{(\mathrm{L})}}{\partial t} = 0. \tag{A7}$$

It is then straight forward to show that:

$$\vec{a}^{(\mathrm{L})}(\vec{r},t) = \frac{e_0}{\omega}\cos\big(\omega t - k_0\, \vec{r}\cdot\vec{u}_\parallel\big)\vec{u}_z, \tag{A8}$$

$$\phi^{(\mathrm{L})}(\vec{r},t)=0. \tag{A9}$$

The small dimensions of the devices studied in this paper allow introducing the *long-wavelength approximation*:

$$\vec{e}(\vec{r},t)\approx e_0\sin(\omega t)\vec{u}_z, \tag{A10}$$

$$\implies \vec{a}^{(\mathrm{L})}(\vec{r},t)\approx\frac{e_0}{\omega}\cos(\omega t)\vec{u}_z. \tag{A11}$$

Finally, a transformation to the velocity gauge is performed with the following gauge transformation function:

$$\chi(t)^{(\mathrm{L}\to\mathrm{vel})}=\frac{e}{2m_e}\int^t \mathrm{d}t'\left(\vec{a}^{(\mathrm{L})}(t')\right)^2 \tag{A12}$$

Because of this transformation, the quadratic term in the vector potential is eliminated and the Hamiltonian reduces to:

$$\hat{h}(t)=\frac{(\hat{\vec{p}})^2}{2m_e}+\frac{e}{m_e}\hat{\vec{p}}\cdot\vec{a}^{(\mathrm{vel})}(t). \tag{A13}$$

In order to compare the semiclassical Floquet-NEGF method to QED-NEGF, the vector potential should be expressed as a function of the photon flux I_ω. To this end, the energy density u_e associated with the impinging plane wave is described classically as:

$$u_e(t)=\frac{\epsilon|\vec{e}(t)|^2}{2}=\frac{\epsilon e_0^2\sin(\omega t)^2}{2}. \tag{A14}$$

By averaging over one period, this becomes:

$$\tilde{u}_e=\frac{\epsilon e_0^2}{4}. \tag{A15}$$

The power flux is then equal to $\tilde{u}_e\,c$, such that the photon flux is found through:

$$I_\omega=\frac{\epsilon e_0^2 c}{4\hbar\omega}. \tag{A16}$$

Finally, in the velocity gauge, we get:

$$\vec{a}^{(\mathrm{vel})}(t)=\sqrt{\frac{4\hbar I_\omega}{\epsilon\omega c}}\cos(\omega t). \tag{A17}$$

Appendix B Floquet-Green equations

Using the two-time Fourier transform (24) in the time-dependent Kadanoff-Baym equations (6)-(7), the following expressions are obtained for the two-energy retarded and lesser Green's functions $\boldsymbol{\mathcal{G}}^{R,<}(E_1,E_1')$:

$$\begin{aligned}&E_1\ \boldsymbol{\mathcal{G}}^R(E_1,E_1')-\int\frac{\mathrm{d}E_2}{2\pi\hbar}\mathbf{H}(E_2)\boldsymbol{\mathcal{G}}^R(E_1-E_2,E_1')\\&=2\pi\hbar\delta(E_1-E_1')\mathbf{I}+\int\frac{\mathrm{d}E_2}{2\pi\hbar}\boldsymbol{\Sigma}^R(E_1,E_2)\boldsymbol{\mathcal{G}}^R(E_2,E_1'),\end{aligned} \tag{B18}$$

$$\begin{aligned}\boldsymbol{\mathcal{G}}^<(E_1,E_1')=\int\frac{\mathrm{d}E_2}{2\pi\hbar}\int\frac{\mathrm{d}E_3}{2\pi\hbar}\boldsymbol{\mathcal{G}}^R(E_1,E_2)\\ \boldsymbol{\Sigma}^<(E_2,E_3)\boldsymbol{\mathcal{G}}^A(E_3,E_1').\end{aligned} \tag{B19}$$

The advanced Green's functions are obtained from the retarded ones through (13), whereas the greater Green's function is not required in the final solution scheme. From (22), the Fourier transform of the time-dependent Hamiltonian in (B18) is given by:

$$\begin{aligned}\mathbf{H}(E)&=2\pi\hbar\,\mathbf{H}_0\delta(E)\\&\quad+2\pi\hbar\frac{A_0\mathbf{p}_z}{2}(\delta(E-\hbar\omega)+\delta(E+\hbar\omega)).\end{aligned} \tag{B20}$$

An expression for the time-dependent current at contact α, $i_\alpha(t)$, is obtained starting from a general time-dependent form of (19) [61]:

$$\begin{aligned}i_\alpha(t_1)=\frac{2e}{\hbar}\int\mathrm{d}t_1'\,\mathrm{Tr}[&\mathbf{g}^R(t_1,t_1')\boldsymbol{\Sigma}_\alpha^<(t_1',t_1)\\&+\mathbf{g}^<(t_1,t_1')\boldsymbol{\Sigma}_\alpha^<(t_1',t_1)\\&-\boldsymbol{\Sigma}_\alpha^R(t_1,t_1')\mathbf{g}^<(t_1',t_1)\\&-\boldsymbol{\Sigma}_\alpha^<(t_1,t_1')\mathbf{g}^A(t_1',t_1)].\end{aligned} \tag{B21}$$

Applying the two-time Fourier transform to the Green's functions and self-energies in (B21) leads

to the following expression:

$$I_\alpha(E) = \frac{2e}{\hbar}\int\frac{\mathrm{d}E_2}{2\pi\hbar}\int\frac{\mathrm{d}E_3}{2\pi\hbar} \mathrm{Tr}[\mathbf{\Sigma}^R_\alpha(E_2,E_3)\boldsymbol{\mathcal{G}}^<(E_3,E_2-E) - \boldsymbol{\mathcal{G}}^R(E_2,E_3)\mathbf{\Sigma}^<_\alpha(E_3,E_2-E) + \mathbf{\Sigma}^<_\alpha(E_2,E_3)\boldsymbol{\mathcal{G}}^A(E_3,E_2-E) - \boldsymbol{\mathcal{G}}^<(E_2,E_3)\mathbf{\Sigma}^A_\alpha(E_3,E_2-E)]. \tag{B22}$$

The periodicity of $\hat{h}(t)$ allows an important simplification of the above equations, based on the following Fourier expansion of all two-energy functions $\boldsymbol{\mathcal{G}}^{R,<}$ into Floquet modes $\mathbf{G}^{R,<}_{m,n}$, which are functions of a single energy variable [40, 62, 63]:

$$\boldsymbol{\mathcal{G}}^{R,<}(E_1,E_1') = 2\pi\hbar\sum_n \mathbf{G}^{R,<}_{0,n}(E_1)\,\delta(E_1'-E_1-n\hbar\omega), \tag{B23}$$

$$\mathbf{G}^{R,<}_{m,n}(E_1) \equiv \mathbf{G}^{R,<}(E_1+m\hbar\omega, E_1+n\hbar\omega). \tag{B24}$$

Similarly, an expansion of the self-energies $\mathbf{\Sigma}^{R/A,\lessgtr}_\alpha$ is possible. However, by assuming that the vector potential disappears in the leads, only the DC-components are retained:

$$\mathbf{\Sigma}^{R/A,\lessgtr}_\alpha(E_1,E_1') = 2\pi\hbar\mathbf{\Sigma}^{R/A,\lessgtr}_\alpha(E_1)\delta(E_1-E_1') \tag{B25}$$

Introducing these Fourier expansions in (B18) and (B19) results in:

$$(E_1\mathbf{I}-\mathbf{H}_0)\mathbf{G}^R_{0,n}(E) - \frac{A_0\mathbf{p}_z}{2}\left(\mathbf{G}^R_{0,n-1}(E)+\mathbf{G}^R_{0,n+1}(E)\right) = \delta_{n,0}\mathbf{I} + \mathbf{\Sigma}^R(E_1)G^R_{0,n}(E_1), \tag{B26}$$

$$\mathbf{G}^<_{0,m}(E) = \sum_n \mathbf{G}^R_{0,n}(E)\mathbf{\Sigma}^<(E+n\hbar\omega)\mathbf{G}^A_{n,m}(E). \tag{B27}$$

For the current, we investigate the DC-component, which corresponds to an average, steady-state value. Substituting (B23) in (B22) results in:

$$I_\alpha(0) = \frac{2e}{\hbar}\int\frac{\mathrm{d}E}{2\pi\hbar}\mathrm{Tr}[\mathbf{\Sigma}^R(E)\mathbf{G}^<_{0,0}(E) - \mathbf{G}^R_{0,0}(E)\mathbf{\Sigma}^<(E) + \mathbf{\Sigma}^<(E)\mathbf{G}^A_{0,0}(E) - \mathbf{G}^<_{0,0}(E)\mathbf{\Sigma}^A(E)]. \tag{B28}$$

To simplify expression (B28), a local equilibrium is assumed in the contacts, such that the *fluctuation-dissipation theorem* can be applied [64]:

$$\mathbf{\Sigma}^<_\alpha(E) = if_\alpha(E)\mathbf{\Gamma}_\alpha(E), \tag{B29}$$

where $f_\alpha(E)$ is the Fermi-Dirac function evaluated with Fermi level μ_α and $\mathbf{\Gamma}_\alpha(E) \equiv i(\mathbf{\Sigma}^R(E) - \mathbf{\Sigma}^A(E))$ is the broadening function. Here, the distinction between $\mathbf{\Sigma}^{R/A}_\alpha$ and the full device-lead coupling self-energy $\mathbf{\Sigma}^{R/A} = \sum_\alpha \mathbf{\Sigma}^{R/A}_\alpha$ is important. Additionally, starting from (9), the following identity holds:

$$\boldsymbol{\mathcal{G}}^A(E_1,E_1) - \boldsymbol{\mathcal{G}}^R(E_1,E_1) = \int\frac{\mathrm{d}E_2}{2\pi\hbar}\int\frac{\mathrm{d}E_3}{2\pi\hbar} [\boldsymbol{\mathcal{G}}^A(E_1,E_2)\mathbf{\Sigma}^A(E_2,E_3)\boldsymbol{\mathcal{G}}^R(E_3,E_1) - \boldsymbol{\mathcal{G}}^A(E_1,E_2)\mathbf{\Sigma}^R(E_2,E_3)\boldsymbol{\mathcal{G}}^R(E_3,E_1)]$$

$$\implies \mathbf{G}^A_{0,0}(E_1) - \mathbf{G}^R_{0,0}(E_1) = \sum_n [\mathbf{G}^A_{0,n}(E)\mathbf{\Sigma}^A(E+n\hbar\omega)\mathbf{G}^R_{n,0}(E) - \mathbf{G}^A_{0,n}(E)\mathbf{\Sigma}^R(E+n\hbar\omega)\mathbf{G}^R_{n,0}(E)]. \tag{B30}$$

Substituting (B27) into (B28), and applying (B29) and (B30), finally results in:

$$\begin{aligned} I_\alpha(0) &= I^{\mathrm{cond}}_\alpha + I^{\mathrm{pump}}_\alpha, \\ I^{\mathrm{cond}}_\alpha &\equiv \frac{2e}{\hbar}\int\frac{\mathrm{d}E}{2\pi}T_{\alpha\beta}(E)(f_\alpha(E)-f_\beta(E)), \\ I^{\mathrm{pump}}_\alpha &\equiv \frac{2e}{\hbar}\int\frac{\mathrm{d}E}{2\pi}(T_{\beta\alpha}(E)-T_{\alpha\beta}(E))f_\alpha(E), \\ T_{\alpha\beta}(E) &\equiv \sum_n \mathrm{Tr}\left[\mathbf{G}^A_{0,n}(E)\mathbf{\Gamma}_\alpha(E+n\hbar\omega)\mathbf{G}^R_{n,0}(E)\mathbf{\Gamma}_\beta(E)\right]. \end{aligned} \tag{B31}$$

References

[1] L. Esaki, R. Tsu, Superlattice and negative differential conductivity in semiconductors. IBM J. Res. Dev. **14**, 61–65 (1970). https://doi.org/10.1147/rd.141.0061

[2] J.P. Sun, G. Haddad, P. Mazumder, J. Schulman, Resonant tunneling diodes: models and properties. Proc. IEEE **86**(4), 641–660 (1998). https://doi.org/10.1109/5.663541

[3] M. Sweeny, J. Xu, Resonant interband tunnel diodes. APL **54**(6), 546–548 (1989). https://doi.org/10.1063/1.100926

[4] S. Zhou, J. Jiang, Q. Cai, Small-signal ac response: a self-consistent non-equilibrium Green's function approach. J. Phys. D: Appl. Phys. **38**(2), 255 (2005). https://doi.org/10.1088/0022-3727/38/2/009

[5] A.M. Fox, Optoelectronics in quantum well structures. Contemp. Phys. **37**(2), 111–125 (1996). https://doi.org/10.1080/00107519608230339

[6] E. Onaran, M.C. Onbasli, A. Yesilyurt, H.Y. Yu, A.M. Nayfeh, A.K. Okyay, Silicon-Germanium multi-quantum well photodetectors in the near infrared. Opt. Express **20**(7), 7608–7615 (2012). https://doi.org/10.1364/OE.20.007608

[7] T. Wood, Multiple quantum well (MQW) waveguide modulators. J. Light. Technol. **6**(6), 743–757 (1988). https://doi.org/10.1109/50.4063

[8] M. Aoki, M. Suzuki, H. Sano, T. Kawano, T. Ido, T. Taniwatari, K. Uomi, A. Takai, InGaAs/InGaAsP MQW electroabsorption modulator integrated with a DFB laser fabricated by band-gap energy control selective area MOCVD. IEEE J. Quantum Electron. **29**(6), 2088–2096 (1993). https://doi.org/10.1109/3.234473

[9] K. Wakita, Y. Kawamura, M. Nakao, H. Asahi, Long wavelength waveguide multiple quantum well optical modulators. IEEE J. Quantum Electron. **23**(12), 2210–2215 (1987). https://doi.org/10.1109/JQE.1987.1073291

[10] M. Koike, N. Shibata, H. Kato, Y. Takahashi, Development of high efficiency GaN-based multiquantum-well light-emitting diodes and their applications. IEEE J. Sel. Top. Quantum Electron **8**(2), 271–277 (2002). https://doi.org/10.1109/2944.999180

[11] W. Lee, M.H. Kim, D. Zhu, A.N. Noemaun, J.K. Kim, E.F. Schubert, Growth and characteristics of GaInN/GaInN multiple quantum well light-emitting diodes. J. Appl. Phys. **107**(6), 063102 (2010). https://doi.org/10.1063/1.3327425

[12] K. Bulashevich, V. Mymrin, S. Karpov, I. Zhmakin, A. Zhmakin, Simulation of visible and ultra-violet group-III nitride light emitting diodes. J. Comput. Phys. **213**(1), 214–238 (2006). https://doi.org/10.1016/j.jcp.2005.08.011

[13] S. Chang, W. Lai, Y. Su, J. Chen, C. Liu, U. Liaw, InGaN-GaN multiquantum-well blue and green light-emitting diodes. IEEE J. Sel. Top. Quantum Electron. **8**(2), 278–283 (2002). https://doi.org/10.1109/2944.999181

[14] J. Faist, F. Capasso, D.L. Sivco, C. Sirtori, A.L. Hutchinson, A.Y. Cho, Quantum Cascade Laser. Science **264**(5158), 553–556 (1994). https://doi.org/10.1126/science.264.5158.553

[15] C. Jirauschek, T. Kubis, Modeling techniques for quantum cascade lasers. Appl. Phys. Rev. **1**(1), 011307 (2014). https://doi.org/10.1063/1.4863665

[16] R.C. Iotti, F. Rossi, Nature of Charge Transport in Quantum-Cascade Lasers. Phys. Rev. Lett. **87**, 146603 (2001). https://doi.org/10.1103/PhysRevLett.87.146603

[17] A. Wacker, Gain in quantum cascade lasers and superlattices: A quantum transport theory. Phys. Rev. B **66**, 085326 (2002). https://doi.org/10.1103/PhysRevB.66.085326

[18] K.W.J. Barnham, G. Duggan, A new approach to high-efficiency multi-band-gap solar cells. J. Appl. Phys. **67**(7), 3490–3493 (1990). https://doi.org/10.1063/1.345339

[19] R. Dahal, B. Pantha, J. Li, J.Y. Lin, H.X. Jiang, InGaN/GaN multiple quantum well solar cells with long operating wavelengths. APL **94**(6), 063505 (2009). https://doi.org/10.1063/1.3081123

[20] L. Kadanoff, G. Baym, *Quantum Statistical Mechanics* (W.A. Benjamin Inc., New York, 1962)

[21] L.V. Keldysh, et al., Diagram technique for nonequilibrium processes. Sov. Phys. JETP **20**(4), 1018–1026 (1965)

[22] J. Schwinger, Quantum Electrodynamics. I. A Covariant Formulation. Phys. Rev. **74**, 1439–1461 (1948). https://doi.org/10.1103/PhysRev.74.1439

[23] E. Perfetto, A. Uimonen, R. van Leeuwen, G. Stefanucci, First-principles nonequilibrium Green's-function approach to transient photoabsorption: Application to atoms. Phys. Rev. A **92**, 033419 (2015). https://doi.org/10.1103/PhysRevA.92.033419

[24] J.S. Wang, N. Zeng, J. Wang, C.K. Gan, Nonequilibrium Green's function method for thermal transport in junctions. Phys. Rev. E **75**, 061128 (2007). https://doi.org/10.1103/PhysRevE.75.061128

[25] R. Tuovinen, R. van Leeuwen, E. Perfetto, G. Stefanucci, Electronic transport in molecular junctions: The generalized Kadanoff–Baym ansatz with initial contact and correlations. Chem. Phys. **154**(9), 094104 (2021). https://doi.org/10.1063/5.0040685

[26] H. Jiang, S. Shao, W. Cai, P. Zhang, Boundary treatments in non-equilibrium Green's function (NEGF) methods for quantum transport in nano-MOSFETs. J. Comput. Phys. **227**(13), 6553–6573 (2008). https://doi.org/10.1016/j.jcp.2008.03.018

[27] W. Wei, L. Jianhui, S. Jianping, G. Ning, Simulation of the electrical characteristics of a one-dimensional quantum dot array. Superlattices Microstruct. **44**(6), 721–727 (2008). https://doi.org/10.1016/j.spmi.2008.09.004

[28] L.E. Henrickson, A.J. Glick, G.W. Bryant, D.F. Barbe, Nonequilibrium-Green's-function theory of transport in interacting quantum dots. Phys. Rev. B **50**, 4482–4496 (1994). https://doi.org/10.1103/PhysRevB.50.4482

[29] N. Neophytou, S. Ahmed, G. Klimeck, Nonequilibrium Green's function (NEGF) simulation of metallic carbon nanotubes including vacancy defects. J. Comput. Electron. **6**, 317–320 (2007). https://doi.org/10.1007/s10825-006-0116-4

[30] W. Wang, X. Yang, N. Li, G. Xiao, S. Jiang, C. Xia, Y. Wang, Transport study of gate and channel engineering on the surrounding-gate CNTFETs based on NEGF quantum theory. J. Comput. Electron. **13** (2014). https://doi.org/10.1007/s10825-013-0499-y

[31] B. Mandal, S. Sarkar, A. Pramanik, P. Sarkar, Electronic structure and transport properties of sulfur-passivated graphene nanoribbons. J. Appl. Phys. **112**(11), 113710 (2012). https://doi.org/10.1063/1.4768524

[32] T. Hossain, M. Rahaman, Band gap tuning and variable quantum barrier of armchair graphene nanoribbons by inducing antidote topologies. J. Comput. Electron. p. 3 (2023). https://doi.org/10.1007/s10825-023-02108-7

[33] U. Aeberhard, R.H. Morf, Microscopic nonequilibrium theory of quantum well solar cells. Phys. Rev. B **77**, 125343 (2008). https://doi.org/10.1103/PhysRevB.77.125343

[34] L.E. Henrickson, Nonequilibrium photocurrent modeling in resonant tunneling photodetectors. J. Appl. Phys. **91**(10), 6273–6281 (2002). https://doi.org/10.1063/1.1473677

[35] N. Dehdashti Akhavan, G.A. Umana-Membreno, R. Gu, J. Antoszewski, L. Faraone, Optimization of Superlattice Barrier HgCdTe nBn Infrared Photodetectors Based on an NEGF Approach. IEEE Trans. Electron Devices **65**(2), 591–598 (2018). https://doi.org/10.1109/TED.2017.2785827

[36] M. Moradinasab, M. Pourfath, M. Fathipour, H. Kosina, Numerical Study of Graphene Superlattice-Based Photodetectors. IEEE Trans. Electron Devices **62**(2), 593–600 (2015). https://doi.org/10.1109/TED.2014.2383354

[37] D. Martinez, Floquet–Green function formalism for harmonically driven Hamiltonians. J. Phys. A Math **36**, 9827 (2003). https://doi.org/10.1088/0305-4470/36/38/302

[38] T.D. Honeychurch, D.S. Kosov, Quantum transport in driven systems with vibrations: Floquet nonequilibrium Green's functions

and the self-consistent Born approximation. Phys. Rev. B **107**(3) (2023). https://doi.org/10.1103/physrevb.107.035410

[39] T.D. Honeychurch, D.S. Kosov, Timescale separation solution of the Kadanoff-Baym equations for quantum transport in time-dependent fields. Phys. Rev. B **100**, 245423 (2019). https://doi.org/10.1103/PhysRevB.100.245423

[40] L. Arrachea, Green-function approach to transport phenomena in quantum pumps. Phys. Rev. B **72**, 125349 (2005). https://doi.org/10.1103/PhysRevB.72.125349

[41] L. Arrachea, M. Moskalets, Relation between scattering-matrix and Keldysh formalisms for quantum transport driven by time-periodic fields. Phys. Rev. B **74**, 245322 (2006). https://doi.org/10.1103/PhysRevB.74.245322

[42] G. Cabra, I. Franco, M. Galperin, Optical properties of periodically driven open nonequilibrium quantum systems. Chem. Phys. **152**(9), 094101 (2020). https://doi.org/10.1063/1.5144779

[43] U.D. Giovannini, H. Hübener, Floquet analysis of excitations in materials. JPhys. Materials **3**(1), 012001 (2019). https://doi.org/10.1088/2515-7639/ab387b

[44] S. Datta, Nanoscale device modeling: the Green's function method. Superlattices Microstruct. **28**(4), 253–278 (2000). https://doi.org/10.1006/spmi.2000.0920

[45] M. Palsgaard, T. Markussen, T. Gunst, Efficient first-principles calculation of phonon-assisted photocurrent in large-scale solar-cell devices. Phys. Rev. Appl. **10**, 014026 (2018). https://doi.org/10.1103/PhysRevApplied.10.014026

[46] U. Aeberhard, Challenges in the NEGF Simulation of Quantum-Well Photovoltaics Posed by Non-Locality and Localization. physica status solidi (b) **256**(7), 1800500 (2019). https://doi.org/10.1002/pssb.201800500

[47] Y. Chang, J.N. Schulman, Modification of optical properties of GaAs-Ga1-xAlxAs superlattices due to band mixing. Appl. Phys. Lett. **43**(6), 536–538 (1983). https://doi.org/10.1063/1.94410

[48] M.P.L. Sancho, J.M.L. Sancho, J. Rubio, Highly convergent schemes for the calculation of bulk and surface Green functions. J. Phys. F Met. Phys. **15**(4), 851 (1985). https://doi.org/10.1088/0305-4608/15/4/009

[49] T.B. Boykin, J.P.A. van der Wagt, J.S. Harris, Tight-binding model for GaAs/AlAs resonant-tunneling diodes. Phys. Rev. B **43**, 4777–4784 (1991). https://doi.org/10.1103/PhysRevB.43.4777

[50] J.A. Driscoll, K. Varga, Calculation of self-energy matrices using complex absorbing potentials in electron transport calculations. Phys. Rev. B **78**, 245118 (2008). https://doi.org/10.1103/PhysRevB.78.245118

[51] M.P. Anantram, S. Datta, Effect of phase breaking on the ac response of mesoscopic systems. Phys. Rev. B **51**, 7632–7639 (1995). https://doi.org/10.1103/PhysRevB.51.7632

[52] G. Stefanucci, S. Kurth, A. Rubio, E.K.U. Gross, Time-dependent approach to electron pumping in open quantum systems. Phys. Rev. B **77**, 075339 (2008). https://doi.org/10.1103/PhysRevB.77.075339

[53] V. Nguyen, J.C. Charlier, Recursive Green's functions optimized for atomistic modelling of large superlattice-based devices. J. Comput. Electron. **22**, 1–16 (2023). https://doi.org/10.1007/s10825-023-02052-6

[54] T.G. Pedersen, K. Pedersen, T. Brun Kriestensen, Optical matrix elements in tight-binding calculations. Phys. Rev. B **63**, 201101 (2001). https://doi.org/10.1103/PhysRevB.63.201101

[55] T.D. Honeychurch, D.S. Kosov, Full counting statistics for electron transport in periodically driven quantum dots. Phys. Rev. B **102**, 195409 (2020). https://doi.org/10.1103/PhysRevB.102.195409

[56] U. Aeberhard, The nonequilibrium Green's function picture of inelastic processes in nanostructure photovoltaics. J. Comput. Electron. **15**, 1219 – 1232 (2016). https://doi.org/10.1007/s10825-016-0877-3

[57] W. Lee, N. Jean, S. Sanvito, Exploring the limits of the self-consistent Born approximation for inelastic electronic transport. Phys. Rev. B **79**, 085120 (2009). https://doi.org/10.1103/PhysRevB.79.085120

[58] J. Pereiro, C. Rivera, A. Navarro, E. Munoz, R. Czernecki, S. Grzanka, M. Leszczynski, Optimization of InGan–GaN MQW Photodetector Structures for High-Responsivity Performance. IEEE J. Quantum Electron **45**(6), 617–622 (2009). https://doi.org/10.1109/JQE.2009.2013140

[59] K.T. Ho, R. Chen, G.L. et al, 3.2 Gigabit-per-second Visible Light Communication Link with InGaN/GaN MQW Microphotodetector. Opt. Express **26**(3), 3037–3045 (2018). https://doi.org/10.1364/OE.26.003037

[60] T. Bilitewski, N.R. Cooper, Scattering theory for Floquet-Bloch states. Phys. Rev. A **91**, 033601 (2015). https://doi.org/10.1103/PhysRevA.91.033601

[61] J. Wang, Time-dependent quantum transport theory from non-equilibrium Green's function approach. J. Comput. Electron. **12**(343-355) (2013). https://doi.org/10.1007/s10825-013-0465-8

[62] B.H. Wu, J.C. Cao, A Floquet–Green's function approach to mesoscopic transport under ac bias. J. Condens. Matter Phys. **20**(8), 085224 (2008). https://doi.org/10.1088/0953-8984/20/8/085224

[63] T. Brandes, Truncation method for Green's functions in time-dependent fields. Phys. Rev. B **56**, 1213–1224 (1997). https://doi.org/10.1103/PhysRevB.56.1213

[64] V. Špička, B. Velický, A. Kalvová, Nonequilibrium dynamics of open systems and fluctuation-dissipation theorems. Fortschritte der Physik **65**(6-8), 1700032 (2017). https://doi.org/10.1002/prop.201700032